Phase diagram of hard spheres confined between two parallel plates

Matthias Schmidt and Hartmut Löwen*
Institut für Theoretische Physik II, Heinrich-Heine-Universität Düsseldorf, Universitätsstrasse 1, D-40225 Düsseldorf, Germany
(Received 24 January 1997)

A hard sphere system confined between two parallel hard plates is investigated theoretically. Using extensive Monte Carlo computer simulations, the phase diagram is calculated for the whole range of densities and plate separations ranging from one to two particle diameters. There occurs a strong first-order fluid freezing transition and both very weak and strong discontinuous phase transitions between different crystal structures, namely, layered, buckled, and rhombic crystals. The results are compared with predictions from free volume theory, and a semiquantitative agreement is found. All predicted transitions should be experimentally observable in confined suspensions of sterically stabilized or highly salted charged colloidal particles. [S1063-651X(97)05606-7]

PACS number(s): 82.70.Dd, 64.70.−p

I. INTRODUCTION

Freezing and melting are phenomena well known from everyday life. Much theoretical as well as experimental work has been devoted to the understanding of the phase transition from a disordered liquid to an ordered, regular solid. The freezing transition can be observed in quite different physical systems, including atomic and molecular systems like iron or water, but also in colloidal suspensions. Usually, colloidal particles appear in a disordered phase constituting a fluid on a mesoscopic length scale. Under appropriate conditions, an ordering of the colloidal particles is also possible, as documented in 1909 by Perrin [1].

Many theoretical studies on freezing focus on bulk properties, neglecting any surface effects. But real systems are generically limited in space. Therefore the effect of confinement on phase transitions is an important issue to address. In fact, this represents an active area of current research. In particular, there exist studies dealing with all phase transitions conceivable for a confined simple liquid. First, the liquid-gas transition in confining geometry which is also called capillary condensation, was investigated; see, e.g., [2,3]. There have been recent studies on a critical fluid confined in between plates focusing on boundary critical phenomena and the Casimir effect [4]. The location of the freezing transition in a capillary [5,6] and in porous materials [7] was studied. Finally, the shift of the dynamical glass transition in confining geometry with respect to the bulk glass transition was also recently measured [8] and calculated [9,10]. We finally mention some peculiar recent results for confined nearly two-dimensional (2D) liquids: First, their dynamics was shown to be close to hydrodynamics with appropriate boundary conditions [11]. Second, stratification-induced transitions were found by computer simulations [12], and the instability of a 2D crystal with respect to buckling waves was demonstrated [13,14].

The present work deals with freezing in confined geometry, with a focus on colloidal suspensions confined between parallel glass plates [15–20], for which our model is particularly designed. The glass plates can be regarded as being smooth on the mesoscopic scale of the colloids. There appears a competition of different length scales, namely, the typical particle extensions and the dimensions of the confinement, which may be commensurate or incommensurate. This leads to multilayered crystals of triangular or square symmetry. Increasing the plate separation distance, the following sequence of crystalline structures was observed experimentally [16–18]:

$$\text{fluid} \rightarrow 1\triangle \rightarrow 2\square \rightarrow 2\triangle \rightarrow 3\square \rightarrow \cdots . \tag{1}$$

The symbol $n\triangle$ denotes n crystal layers with triangular (also called hexagonal) symmetry, equivalent to the structure of (111) planes in a fcc crystal n. Layers with fourfold rotational symmetry, equivalent to (110) planes, are denoted by a $n\square$ symbol. The experiments have mainly been carried out in a wedge geometry. An advantage of the wedge geometry is the continuous range of plate separation distances. The drawback, on the other hand, is the introduction of an additional degree of freedom, namely, the wedge angle. Only in the case of small wedge angles can the plates be regarded as locally parallel.

Quite early, there were also ''mazelike'' patterns observed [21] that do not fit into the simple sequence (1). One main result of the present work is that *more phases are thermodynamically stable*, and that their succession is more complicated, depending sensitively on the density and plate separation distance.

Let us briefly mention further setups where nearly two-dimensional fluids are realized: First, thin films of colloidal suspension can also be produced by spreading the suspension over a solid substrate. For different experimental investigations of ordered colloidal structures on solid substrates, see [22–24]. Second, at an air-water interface, colloidal particles can be trapped [25]. The emerging soft repulsive interaction of aligned dipoles leads to formation of a two-dimensional (2D) crystal [26,27]. Last, freezing in few layers of a dusty plasma has been studied [28–30] and considerable attention has been devoted also to the behavior of confined 2D electrons; see, e.g., Refs. [31–36].

*Also at Institut für Festkörperforschung, Forschungszentrum Jülich, D-52425 Jülich, Germany.

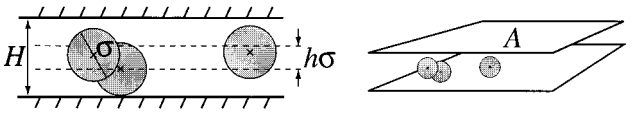

FIG. 1. Hard spheres of diameter σ confined between parallel hard plates with area A and plate separation distance H.

The aim of our paper is to study theoretically the phase diagram of the simple model of hard spheres confined between hard plates. Despite its simplicity, the resulting phase diagram is rich, allowing for the stability of fluid as well as different crystalline phases. The actual crystalline phases can be more complicated than a simple sequence of $n\triangle$ or $n\square$ layers. In particular we find stable *buckled* and *rhombic* crystals. Our results are based upon Monte Carlo simulations and a simple free volume theory. Parts of the results have already been published elsewhere [37].

The paper is organized as follows: In Sec. II, we introduce the model and discuss its limiting cases. In Sec. III, we describe the Monte Carlo simulation technique. The results are presented in Sec. IV. Furthermore, in Sec. V, we discuss the free volume theory. Finally, Sec. VI is devoted to concluding remarks.

II. MODEL: HARD SPHERES BETWEEN HARD PLATES

A. Model and notation

Our model system consists of N hard spheres of diameter σ confined between parallel hard plates with area A and gap thickness $H=(h+1)\sigma$, such that $h=0$ corresponds to the 2D limit of hard disks; see Fig. 1. The pair interaction potential between particles with position vectors $\mathbf{r}$ and $\mathbf{r}'$ depends on the magnitude $r=|\mathbf{r}-\mathbf{r}'|$, and is given by

$$V(r)=\begin{cases}0 & \text{if} \quad r\geqslant\sigma \\ \infty & \text{if} \quad r<\sigma.\end{cases} \tag{2}$$

The confining hard walls are modeled by an external potential

$$V_{\text{ext}}(\mathbf{r})=\begin{cases}0 & \text{if} \quad -h\sigma/2\leqslant z\leqslant +h\sigma/2 \\ \infty & \text{otherwise,}\end{cases} \tag{3}$$

where z is the component of the vector $\mathbf{r}$ perpendicular to the plates. The total potential energy is

$$V_{\text{pot}}(\mathbf{r}_1,\ldots,\mathbf{r}_N)=\sum_{i=1}^{N}\sum_{j=i+1}^{N}V(|\mathbf{r}_i-\mathbf{r}_j|)+\sum_{i=1}^{N}V_{\text{ext}}(\mathbf{r}_i). \tag{4}$$

Since temperature is irrelevant for excluded-volume interactions, the only thermodynamic quantities are the reduced particle density $\rho_H=N\sigma^3/(AH)$ and the effective reduced plate separation h. In the limit $h\to 0$ the third dimension can be neglected, and we end up with 2D hard disks. In the opposite case $h\to\infty$, the effect of the confining plates vanishes, and the 3D bulk hard sphere system is recovered.

With the Helmholtz canonical free energy denoted by F, we define two different pressures of the systems:

$$P_{\text{lat}}=-H^{-1}\left.\frac{\partial F}{\partial A}\right|_{H,N,T}, \tag{5}$$

$$P_{\text{trans}}=-A^{-1}\left.\frac{\partial F}{\partial H}\right|_{A,N,T}. \tag{6}$$

The corresponding reduced pressures are

$$p_{\text{lat}}=\sigma^3 P_{\text{lat}}, \tag{7}$$

$$p_{\text{trans}}=\sigma^3 P_{\text{trans}}. \tag{8}$$

The wall theorem [38] relates the transversal pressure to the one-particle density field $\rho(\mathbf{r})$ as follows:

$$\overline{\rho(z)}=\frac{1}{A}\int dx\ dy\ \rho(\mathbf{r}) \tag{9}$$

$$\beta P_{\text{trans}}=\overline{\rho(\pm h/2)}. \tag{10}$$

Phase coexistence implies the equality of the lateral pressures and the chemical potentials in the two coexisting phases. Note that the equality of temperature is trivial for hard bodies.

B. Bulk limits of the model: 3D and 2D

In the limit $h\to\infty$ at fixed density ρ_H, we encounter the 3D bulk hard sphere system which undergoes a strongly first-order freezing transition. The coexisting fluid and solid volume fractions are $\eta_{\text{f}}=0.494$ and $\eta_{\text{s}}=0.545$. The crystalline structure of the solid phase is close packed, although it is unknown which close-packed structure is the thermodynamically stable one.

As a different limiting case for $h\to\infty$, one can keep the position of one plate fixed, and remove the other plate to infinity. Then the hard sphere system at a single wall is obtained. This situation represents the basic inhomogeneity for hard spheres, as no additional parameter with respect to the bulk system is introduced. One can study density profiles [39,40] and correlation functions [41] within density-functional theory or integral equation theory [42,43]. As concerns the solid phase, density profiles and surface tensions have been calculated by density-functional theory [44]. A precrystallization effect induced by the presence of the wall was found [44–46], showing the wetting of a single wall by close-packed (111) fcc planes.

The fluid phase in slab geometry was investigated in the grand-isostress ensemble [47] by computer simulation, and correlation functions and density profiles were calculated within density-functional theory [48]. Also the freezing transition between plates was investigated focusing on large plate separations [49]. Dynamical aspects were studied in Refs. [50,51].

The 2D case of hard disks is obtained by letting $h\to 0$ at fixed density ρ_H. While it is established that the 2D hard disk system undergoes a freezing transition (unlike the 1D hard rod model), the nature of two-dimensional melting is a current area of research (see Ref. [52] for a review). Basically, there are two main scenarios: Similar to the 3D case, there could occur a first-order freezing transition with a finite

density jump. Alternatively there is the celebrated Kosterlitz-Thouless-Halperin-Nelson-Young scenario, consisting of two continuous phase transitions (i.e., with vanishing density discontinuity) from the liquid to the so-called hexatic phase, and a further phase transition from the hexatic phase to the 2D crystal. Although recent studies are still controversial [53–55], there is now more and more compelling evidence for the fact that the hard-disk freezing transition is first order [56,57].

C. Low- and high-density limits of the model

1. Ideal gas

The statistical physics of N noninteracting particles inside a given volume V is governed by the number density and the thermal energy k_BT alone. We show how the results for two and three dimensions are recovered as special cases if the particles are confined in a volume with area A and height $h\sigma \equiv H-\sigma$. The free energy per particle is

$$f_{\rm id}=k_BT\left[\ln\left(\frac{N\Lambda^3}{Ah\sigma}\right)-1\right], \tag{11}$$

where $\Lambda=\sqrt{h^2/2\pi m k_BT}$ is the thermal de Broglie wavelength. The ideal pressures are

$$\beta p_{\rm lat}=\rho_H, \tag{12}$$

$$\beta p_{\rm trans}=\frac{h+1}{h}\rho_H. \tag{13}$$

The prefactor $(h+1)/h$ is due to the definition of the density ρ_H. The 3D limit is obtained by letting $h\to\infty$, such that $\rho_{\rm 3D}=N/(Ah\sigma)$ is kept constant,

$$\beta f_{\rm id}^{\rm 3D}\equiv\lim_{h\to\infty}\beta f_{\rm id}=\ln(\rho_{\rm 3D}\Lambda^3)-1. \tag{14}$$

For the case of a 2D classical ideal gas, a regularization is needed. We let $h\to 0$, while keeping the 2D area density fixed, $\rho_{\rm 2D}=N/A$, and subtract the diverging contribution to obtain

$$\beta f_{\rm id}^{\rm 2D}\equiv\lim_{h\to 0}\left[\beta f_{\rm id}-\ln\frac{\Lambda}{h\sigma}\right]=\ln(\rho_{\rm 2D}\Lambda^2)-1. \tag{15}$$

2. Virial expansion

Virial coefficients for hard disks are known analytically and numerically [58,59]. In an inhomogeneous system, the virial coefficients become *functions* of the external parameters, in our case on the plate separation distance h. Computing the second virial coefficient yields the first correction to the excess free energy. Written in reduced units, the virial expansion of the excess free energy per particle for the case $h<1$ is explicitly given by

$$\beta f_{\rm ex}=\frac{\pi}{2}\rho_{\rm 2D}\sigma^2\left(1-\frac{h^2}{6}\right), \tag{16}$$

where $\rho_{\rm 2D}=N/A$. The virial corrections to the pressures defined in Eqs. (6) and (5) are

$$\frac{\beta p_{\rm lat}}{\rho_H}=1+\frac{\pi}{2}\rho_H(1+h)\left(1-\frac{h^2}{6}\right)+O(\rho_H^2), \tag{17}$$

$$\frac{h}{h+1}\frac{\beta p_{\rm trans}}{\rho_H}=1+\pi\rho_H(1+h)\frac{h^2}{6}+O(\rho_H^2). \tag{18}$$

3. Close packing

As described above for the 2D and 3D bulk limits, the hard sphere system freezes into respective close-packed structures. Considering hard spheres confined between plates it is therefore natural to ask for the close-packed structure which provide the high-pressure limit of our model. This was considered by Pansu, Pieranski, and Pieranski [60].

Stacking n layers of square or triangular symmetry gives candidate close-packed structures at discrete values of plate separation distance h. These packings can be considered as slabs of a (close-packed) 3D fcc crystal. The slabs are parallel to lattice planes with small indices as the (111) direction (here called triangular layer, △) or (110) direction (square layer, □). For n stacked square layers the density ρ_H at discrete plate separation distances h is given by

$$\rho_H(n\square)=\frac{\sqrt{2}}{1+(\sqrt{2}-1)/n}, \tag{19}$$

$$h(n\square)=(n-1)/\sqrt{2}. \tag{20}$$

In the case of n triangular layers, the values are

$$\rho_H(n\triangle)=\frac{\sqrt{2}}{1+(\sqrt{3/2}-1)/n}, \tag{21}$$

$$h(n\triangle)=\sqrt{\tfrac{2}{3}}(n-1). \tag{22}$$

Of course, in the limit of $n\to\infty$ both solutions approach the density of a close-packed 3D fcc crystal, namely, $\rho_H(\text{ fcc})=\sqrt{2}$. For small values of n, these structure are expected to be close packed, but for $n\gtrsim 5$ distorted triangular layers may be more dense than the $n\square$ crystal, even at plate separations $h(n\square)$.

Quite surprisingly, there are several crystalline structures known to exist that interpolate *continuously* between square and triangular layers. One complete sequence of close-packed structures connecting $1\triangle$ via $2\square$ to $2\triangle$ is depicted in Fig. 2. The crystal interpolating between $1\triangle$ and $2\square$ is called the buckling structure, that between $2\square$ and $2\triangle$ the rhombic phase. The densities of these sphere packings were calculated in Ref. [60]. For the buckling structure (b) interpolating between $1\triangle$ and $2\square$ for $0\leqslant h\leqslant 1/\sqrt{2}\approx 0.707$, the density is given by

$$\rho_{\rm CP}(h)=\frac{2}{(h+1)\sqrt{3-4h^2}}. \tag{23}$$

The rhombic crystal (r), which is close packed for $0.707\approx\sqrt{1/2}\leqslant h\leqslant\sqrt{2/3}\approx 0.816$ interpolating between $2\square$ and $2\triangle$ layers, has a density

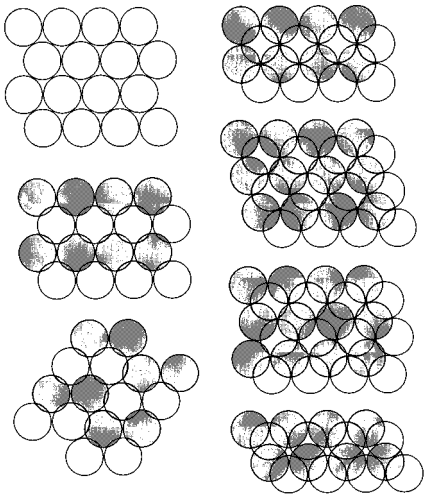

FIG. 2. The various close-packed structures. Left column: $1\triangle$, linear buckling, zigzag buckling. Right column: $2\square$, linear rhombic, zigzag rhombic, $2\triangle$ (from top to bottom). Spheres from the lower layer are dark shaded, while spheres from the upper layer are transparent.

$$\rho_{\mathrm{CP}}(h)=\frac{4(1-h)}{\sqrt{3-4h^2}}. \tag{24}$$

Here we note that buckling structures appear not only as a perturbation of a 2D crystal [13,14], but are present in quite different physical systems, as amphiphilic membranes [61–63] or Langmuir films [64]. Both the buckling and the rhombic structure are highly degenerate. Each of them may appear in three forms: The strictly periodic linear and zig-zag structures are depicted in Fig. 2, but a random alternation of both is also conceivable and does not cost packing volume. The situation is quite similar to that in three dimensions, where we have the degeneracy of close packing with respect to the stacking sequence.

As regards larger plate separations with $n\geqslant 3$ layers, the problem of the densest sphere-packing becomes increasingly complicated as many other candidate packings have to be taken into account. First, there are the two prism structures [65,20] interpolating between n and $n+1$ square layers, and interpolating between $n\triangle$ and $(n+1)\triangle$. The latter case reduces for $n=1$ to the buckling structure. Second, there is the n-layered rhombic structure, that interpolates between $n\square$ and $n\triangle$ layers. Third, there is a structure interpolating between $n\triangle$ and $3n\triangle$ via division of each $\triangle$ layer into three triangular sublattices (see Fig. 11a of Ref. [60]). This structure is not close packed for the $1\triangle$-$3\triangle$ transition.

III. MONTE CARLO SIMULATION TECHNIQUES

We performed a standard canonical NVT ensemble simulation [66]. The number of particles N ranges typically from $N=192$ to 4608 to check systematically for finite-size effects. Particle coordinates are analyzed to obtain the lateral pressure as a function of density, and hence the equation of state, from which phase coexistence is determined by Maxwell's construction equating lateral pressures and chemical potentials. Compression and expansion runs have been compared in order to check for sufficient equilibration. As a consistency check, we also used the single occupancy cell method [67,68] (see also [69]) for $h=0.85$, finding the same phase boundaries.

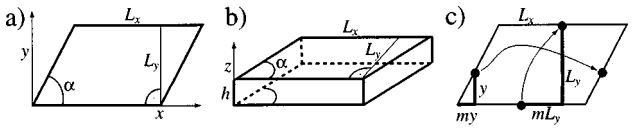

FIG. 3. Shape of the simulation box: (a) parallelogram in the lateral plane; (b) 3D view of the box; (c) periodic boundary conditions, and identification of boundary points.

Periodic boundary conditions in lateral direction are implemented using a parallelogram-shaped box that varies its shape during the simulation. This is necessary to make it possible for any crystal structure to fit in the simulation box.

The ground area of the simulation box in the lateral xy plane is a parallelogram with angle α, aspect ratio $q=L_y/L_x$, and area $A=L_xL_y$, see Fig. 3(a). Perpendicular to the parallelogram the box has the height h. A 3D view of the simulation box is plotted in Fig. 3(b). The box aspect ratio $q=L_y/L_x$ and angle α vary in the course of the simulation to allow for a structural rearrangement of the system. After each system update (one attempted move per particle) one box Monte Carlo move is done. This collective move consists of the following steps: First, one generates randomly new trial values q' and α'. Then the box and particle coordinates are updated to fit into the new box shape. Finally, the nonoverlap criterion is checked and, depending upon the result, the new configuration is accepted or rejected. There is a ''squeezing'' move, that changes q at constant α and there is a ''shearing'' move, that changes the angle α at constant box aspect ratio q.

While the transversal pressure is obtained via the wall theorem, the lateral pressure is efficiently calculated by using the probability density of a successful infinitesimal rescaling of all lateral coordinates with unchanged z coordinates. See Appendix A for more technical details.

IV. MONTE CARLO RESULTS

A. Phase diagram

In Fig. 4 the Monte Carlo data for the phase diagram is shown as a function of density ρ_H and plate separation distance h [37]. The different system sizes are denoted by different symbols, indicating that the dependence on system size is only weak. Altogether there are six thermodynamically stable phases: fluid phase (f), one triangular crystal layer $(1\triangle)$; buckling phase (b), two square crystal layers $(2\square)$; rhombic phase (r), two triangular crystal layers $(2\triangle)$. At the left (low-density) side, the phase diagram is enclosed by the fluid phase; at the right (high-density) side it is limited by the close-packed states residing on the dashed line given by Eqs. (23) and (24). Between the fluid and the forbidden region there are five crystal phases, whose relative stabilities are determined by the density and the plate separation distance.

In Fig. (5) the phase diagram is shown using the lateral pressure instead of the density as free thermodynamic vari-

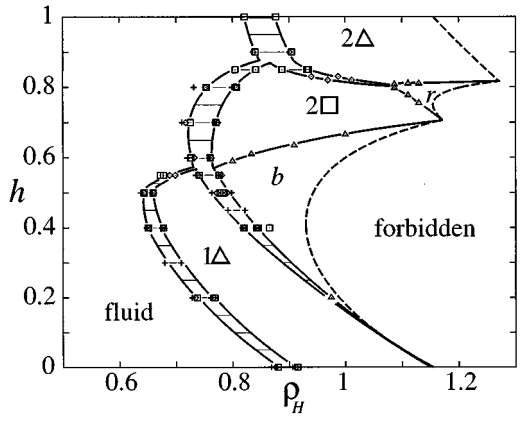

FIG. 4. Monte Carlo result for the phase diagram of hard spheres of density ρ_H confined between parallel plates with separation distance h: $N=192$ (+); 384,512 (◇); 576 (△); and 1024, 1156 (□). Solid lines are guides to the eye. Thin horizontal lines represent two-phase coexistence. See also Fig. 16.

able. The close-packed states are shifted to infinite lateral pressures. Coexistence density intervals collapse onto lines. The freezing transition is observed to appear around $p_{\rm lat}=7-9$. Detailed numerical data for all transitions are given in Ref. [70]. Let us discuss some features of the transitions in more detail.

(i) Fluid-1△, $0<h<0.57$. For $h=0$ we recover the first-order freezing transition of the hard disk fluid into one triangular crystal layer. The same phase transition also occurs for finite values of h up to $h=0.55$. The f-1△ transition vanishes at $h=0.57$ with a triple point $(f,1\triangle,b)$.

(ii) 1△-buckling, $0<h<0.57$. In the same h interval as the f-1△ transition, we find that upon increasing the density a structural phase transition occurs from one triangular layer (1△) to the buckling phase (b), which is stable up to close packing. For values of h close to zero the phase transition is shifted to high densities and disappears for $h=0$.

(iii) Fluid-2□, $0.57<h<0.86$. In the interval $0.57<h<0.86$ the fluid freezes into two square crystal layers (2□). Again the boundaries of the h interval are gained by extrapolation. The density discontinuity is larger than for freezing into the triangular layer.

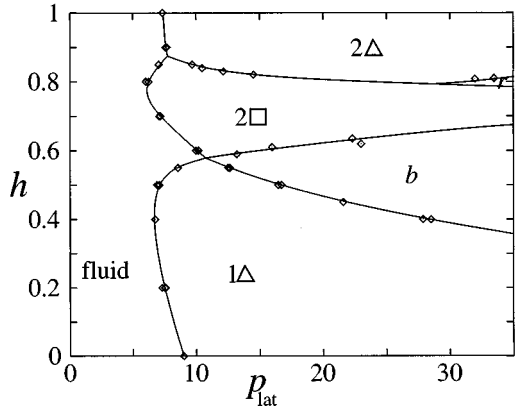

FIG. 5. Same as Fig. 4, but using the lateral pressure instead of the density as the free thermodynamic variable. The reduced pressure is given in units of k_BT.

(iv) 2□-b, $0.57<h<0.71$. By accident the triple point $(f,2\square,b)$ lies within statistical uncertainty at the same value of $h=0.57$ as the triple point $(f,1\triangle,b)$. Therefore we cannot resolve whether the former occurs at a higher plate separation, implying a fluid-buckling transition, or at a lower separation, implying a 1△-2□ transition. The upper bound of the interval $h=\sqrt{1/2}\approx 0.71$ is again obtained by plausible extrapolation to the lines of close packing. It should be emphasized that the buckling crystal is only stable at values of h where it also constitutes the close-packed structure. As it turns out, the order of the 2□-b transition is an interesting and very subtle question. For its investigation, we will consider the finite-size dependence of the order-parameter fluctuations in Sec. IV B.

(v) 2□-r, $0.71<h<0.8$. The data for phase transitions to the rhombic phase are gained by considering the behavior of the order parameters; see Sec. IV B. No anomalies in the equation of state could be detected. The Monte Carlo runs were performed at constant ρ_H and varying plate separation h. By analogy we conclude that the order of the 2□-r transition should be equal to the order of the 2□-b transition.

(vi) 2□-2△, $0.8<h<0.86$. A pronounced density jump separates the 2□ from the 2△ phase.

(vii) 2△-r, $0.8<h<0.81$. An almost horizontal 2△-r coexistence region is observed.

(viii) Fluid-2△, $0.86<h<1$. For the largest plate separation distances considered in this study, we find a strong discontinuous freezing transition to two crystalline layers.

B. Order parameters Ψ_{mn}

In order to identify the emerging crystalline phases, we introduce a set of double-indexed order parameters Ψ_{mn} defined via

$$\Psi_{mn}\equiv\left\langle N^{-1}\sum_{\alpha=1}^{N}|\Psi_n(\alpha)|\exp[im\ \arg\Psi_n(\alpha)]\right\rangle, \quad (25)$$

$$\Psi_n(\alpha)\equiv N_\alpha^{-1}\sum_\beta \exp(in\Theta_{\alpha\beta}). \quad (26)$$

Here $\langle\ \rangle$ denotes a canonical average, and the sum is over N_α neighbors of particle α possessing lateral distances smaller than 1.2σ and having opposite signs in their z coordinates, $\Theta_{\alpha\beta}$ is the angle between the bond of particles α and β and an arbitrary axis.

The fluctuations of the order parameters are measured by means of an order parameter susceptibility

$$\chi_{mn}(N)=N(\langle|\Psi_{mn}|^2\rangle-\langle|\Psi_{mn}|\rangle^2) \quad (27)$$

depending on the particle number N. It will be used to investigate the order of weak phase transitions [56,57] (see also [71]).

Apart from free energy calculations, phase boundaries also can be calculated from a knowledge of the dependence of the order parameters Ψ_{mn} on the variables ρ_h and h. An abrupt change in the order parameter signals a phase transition. This procedure proves useful in cases where there is no

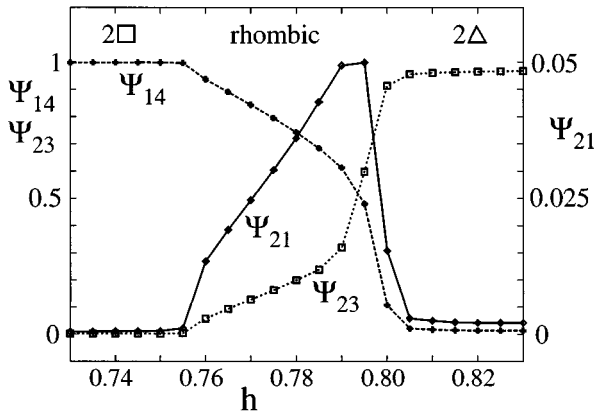

FIG. 6. Behavior of the order parameters Ψ_{14}, Ψ_{21}, and Ψ_{23} in three different phases ($2\square$, r, and $2\triangle$) vs h for $\rho_H = 1.134$.

significant anomaly in the equation of state observed, hence for very weak first-order and second-order phase transitions. We relied on that technique for the calculations of the $2\triangle$-r, $2\square$-r, and $2\square$-b phase boundaries (see Fig. 6). Once the phase boundaries are determined, from knowledge of the order parameter susceptibility χ_{mn} the order of the phase transition can be concluded. The following two cases are conceivable: (i) If a phase transition were *continuous* in the thermodynamic limit $N\rightarrow\infty$, diverging fluctuations would be observed at the critical point, and $\chi_{mn}(\rho_H\rightarrow\rho_H^{\rm crit})\rightarrow\infty$. Of course, diverging fluctuations are encountered only in the thermodynamic limit, which is not directly accessible in computer simulations. Hence we study the dependence of χ_{mn} on the system size N, and look for an emerging singularity as the system becomes larger. (ii) In the *discontinuous* case, where the correlation length remains finite, entering the coexistence region would simply mix the susceptibilities of the coexisting phases according to the relative weight of both phases $\chi_{mn}(\rho_H)=\lambda\chi_{mn}(\rho_H^{(1)})+(1-\lambda)\chi_{mn}(\rho_H^{(2)})$, where the superscripts 1 and 2 stand for the low- and high-density coexisting phases, and $\lambda=(\rho_H^{(1)}/\rho_H^{(2)})\ (\rho_H^{(2)}-\rho_H)/(\rho_H^{(2)}-\rho_H^{(1)})$ is the ratio of the number of particles in phase 1 to the total number of particles in both phases. The functional dependence of χ_{mn} on ρ_H is linear, no divergence is encountered. See Appendix B for a discussion of different ensembles.

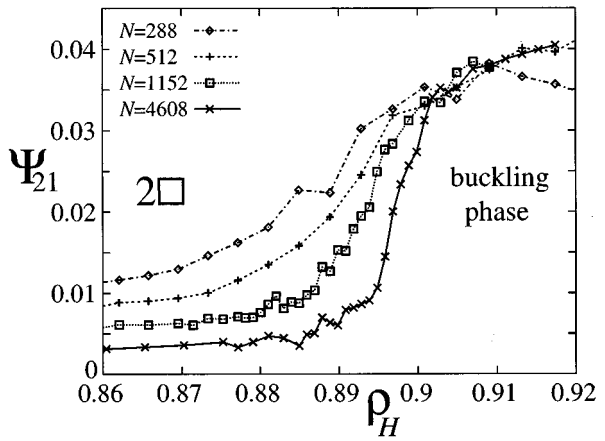

FIG. 7. Behavior of the order parameter Ψ_{21} across $2\square$—the buckling phase boundary at $h = 0.62$.

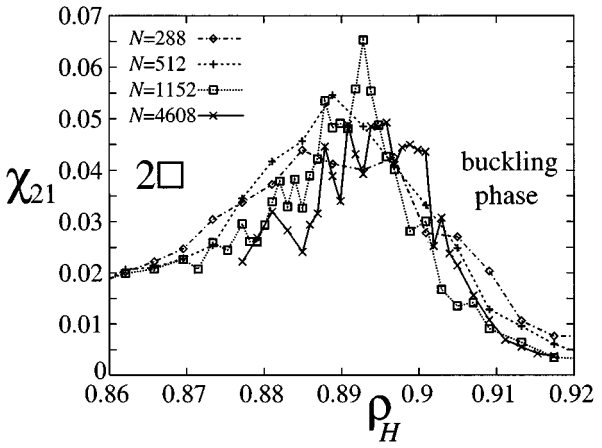

FIG. 8. Order parameter susceptibility χ_{21} as a function of density ρ_H at plate separation distance $h = 0.62$. No divergence of the maximal value as a function of particle number N is observed.

Let us now examine the $2\square$-b transition in detail, using finite-size scaling of the order parameter susceptibility. For the investigation of the $2\square$-b transition the quantity Ψ_{21} ($m=2, n=1$) is useful, as it is larger than zero for ''kite''-shaped particle arrangements (present in the zigzag or random buckling phase) and vanishes for the square configurations (exhibited typically in stacked $n\square$ phases).

The order parameter Ψ_{21} is shown in Fig. 7 for fixed plate separation distance $h = 0.62$ as a function of density ρ_H. The function $\Psi_{21}(\rho_H)$ increases in a relative small density interval $\rho_H = 0.87-0.9$ from a value close to zero to a finite value of about 0.04. We find that the fluctuations on the low-density side vanish with a $1/\sqrt{N}$ size dependence in the thermodynamic limit $N\rightarrow\infty$. We thus conclude, that the $2\square$ phase is thermodynamically stable for low densities. In contrast, on the high-density side, no decrease of Ψ_{21} as a function of particle number N is observed; from the date for finite-size systems we can conclude that a value significantly greater than zero is reached as $N\rightarrow\infty$. The buckling structure with only twofold rotational symmetry is present. Hence a phase transition occurs between $2\square$ and b, signaled by a rapid increase of the order parameter Ψ_{21} as a function of density ρ_H. As a function of N, the increase is more rapid (with a larger slope) and is shifted toward higher densities.

In Fig. 8 the susceptibility χ_{21} as a function of density ρ_H is shown for the plate separation distance $h = 0.62$. The susceptibility has small values in the low-density $2\square$ phase and in the high-density buckling phase. Between the pure

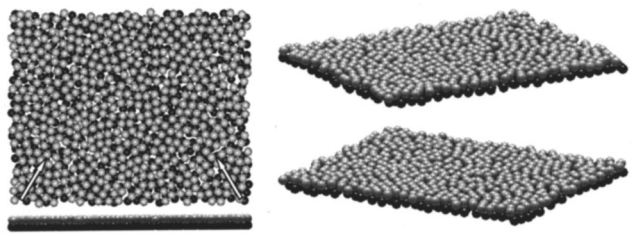

FIG. 9. Fluid phase (f); $h = 0.9$ and $N = 1056$.

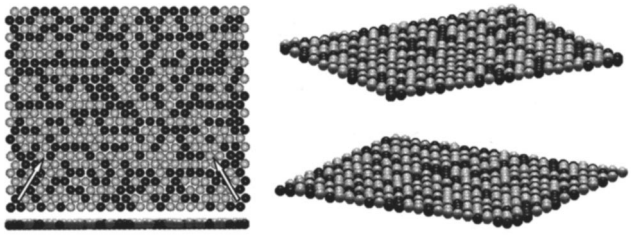

FIG. 10. One triangular crystal layer ($1\triangle$); $h=0.2$ and $N=576$.

phases a pronounced maximum occurs that can be interpreted in terms of fluctuations driving the system from one phase to the other. In contrast to the finite-size dependence of the order parameter itself, its susceptibility shows only a weak dependence on system size. Although statistical errors are present, there is no indication up to $N=4608$ of a divergence in the thermodynamic limit. We thus conclude that the phase transition between the $2\square$ and the buckling structure is of first order. The density jump is smaller than the resolution of the simulation $\Delta\rho_H=0.001$.

C. Typical configurations of six phases

In the following we present snapshots of typical particle configurations generated by Monte Carlo simulation. The particles are depicted in two different shades to emphasize their position in the z direction: Particles from the upper half-space (with positive z coordinates) are light shaded, while particles from the lower half-space (with negative z coordinates) are dark shaded.

In the sequence of plots (9)–(14) each configuration is shown four times: The main picture in the top left corner is a view perpendicular to the walls illustrating the lateral order. Below it there is a side view which demonstrates the thickness of the confined system. On the right side of each figure two perspective views are shown, which are seen along the white arrows in the main picture (top left). The upper perspective view corresponds to the left arrow, the bottom one to the right arrow. Both views are seen under an azimuthal angle of $-15°$. For the buckling (b) and the rhombic (r) phases (Figs. 11 and 13) the two projections do differ qualitatively, while they are similar for the more symmetric phases (f, $1\triangle$, $2\square$, and $2\triangle$). In all cases *defect-free* configurations are chosen. Also, for plotting convenience, configurations with box aspect ratios away from unity (equilateral) were chosen. We now briefly discuss the typical features of each configuration.

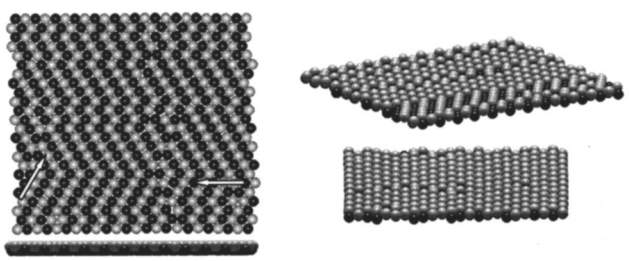

FIG. 11. Buckling phase (b) at $h=0.4$ and $N=576$.

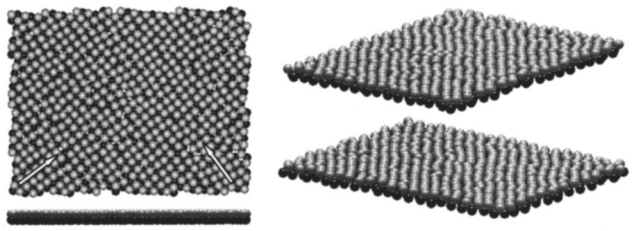

FIG. 12. Two square crystal layers ($2\square$); $h=0.85$ and $N=1056$.

(i) Fluid phase (f), Fig. 9. Neither translational nor orientational ordering is observed. The particles are located preferentially near one of the walls.

(ii) One triangular crystal layer ($1\triangle$ phase), Fig. 10. At higher density the system freezes into a lateral ordered lattice. The up-down symmetry is unbroken, the particles being randomly distributed in z coordinates.

(iii) Buckling phase (b), Fig. 11. Ordering in the z direction sets in: There are meandering lines of upper and lower particles. The lateral structure is a distorted $1\triangle$ lattice, and the perspective views are no longer equivalent. Symmetry breaking occurs, the system now having only twofold rotational symmetry.

(iv) Two square crystal layers ($2\square$ phase), Fig. 12. A fourfold rotational symmetry is recovered.

(v) Rhombic phase (r), Fig. 13. The structure is not only a distorted $2\square$ lattice, but constitutes an individual phase. Symmetry breaking has occurred, so that the two crystal directions are no longer equivalent.

(vi) Two triangle crystal layers ($2\triangle$ phase), Fig. 14. A sixfold (threefold) rotational symmetry is present. This structure can be obtained by diffusive rearrangement of particles from the (r) phase.

V. FREE-VOLUME THEORY

In this section we propose a simple theory for the confined hard sphere system, consisting of a cell model approach to the crystalline phases and an effective-disk diameter approach based on the Born-Green-Yvon hierarchy to the confined fluid phase. Both approaches are subsumed under the term free-volume theory, as they are characterized by stringent approximations to the interparticle correlations and focus on the free volume accessible to a single particle.

A. Cell model for crystalline phases

The cell model [72–75] exploits the physical picture of a solid, with particles localized around given lattice sites. It

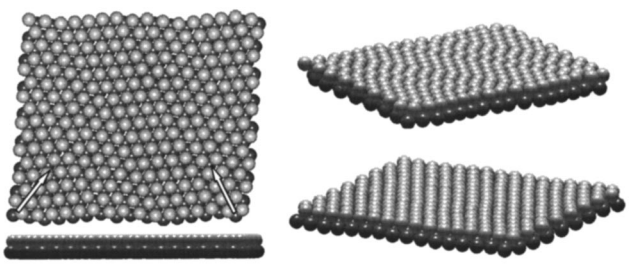

FIG. 13. Rhombic phase (r).

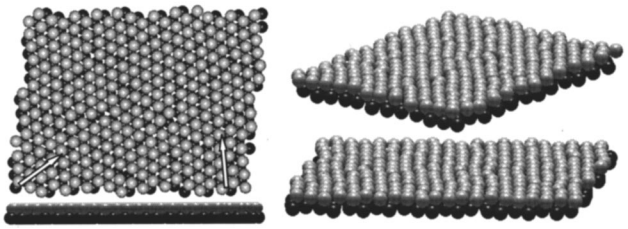

FIG. 14. Two triangular crystal layers (2△); $h=0.85$ and $N=576$.

enables one to determine the thermodynamically stable crystalline structure and its equation of state approximately. Furthermore, it provides an exact upper bound on the free energy. The cell model has been applied in various contexts, including glasses [76] and systems displaying rotational degrees of freedom [77,78]. Despite the relative simplicity of the model, for the 3D hard sphere crystal the predicted equation of state yields remarkable agreement with simulation, especially at high densities (see also [79] for comparison with density-functional theory, and [80] for a discussion of high-density properties, as well as [81] for a similar approach). Also in the context of confined hard spheres, some solid-to-solid transitions have been calculated [72] within the cell model approach.

Applying the cell model to our system, we first impose a candidate lattice structure, given by a set of lattice sites $\{\mathbf{R}_i\}$, compatible with the overall density ρ_{H} and plate separation H. In general, this structure will depend on a set of free geometric parameters, $\mathbf{R}_i(\{a_j\})$, the a_j being angles, ratios of lattice constants, etc. Second, the integration regime of each particle in the configurational integral is restricted from the total volume V to a smaller region in space around each lattice site $\mathbf{R}_i$, called the free-volume cell V_i. With v_{f} being the spatial volume of one cell, the expression $-k_BT\ln(v_{\mathrm{f}}/\Lambda^3)$ provides an upper bound on the exact (Helmholtz) free energy per particle. To optimize this bound, we minimize it with respect to the set of free parameters $\{a_j\}$.

The calculation of the free-volume cell involves tedious elementary geometrical considerations. The volume of the cell has to be calculated for any given crystalline structure. Via elementary geometrical calculus we obtain an *analytical* expression for the free volume v_f for the 1△, b, and 2□ phases. It is given by

$$v_{\mathrm{f}}/\sigma^3=\frac{h+1}{96v_H d}\left[\sum_{i=0}^{3}\Theta(x_{+,i})x_{+,i}^3-\sum_{i=0}^{3}\Theta(x_{-,i})x_{-,i}^3\right], \tag{28}$$

$$f=-k_BT\ln(v_f/\Lambda^3), \tag{29}$$

$$v_H=\rho_H^{-1}=a_1a_2(1+h)/2, \tag{30}$$

where Θ denotes the Heaviside step function, and

$$x_{\pm,i}=P_{\pm,i}-\sqrt{b_1^2+b_2^2+d^2}. \tag{31}$$

We have defined scaled lattice constants $b_1=a_1/2$ and $b_2=a_2/2$, and d is the scaled distance between the two layers ($d<h$), see Fig. 15. The coefficients $P_{\pm,i}$ are given by

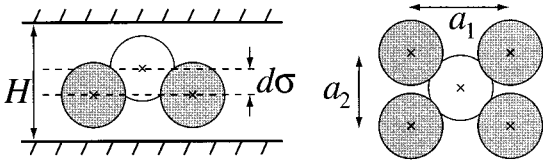

FIG. 15. Lattice constants of the buckling structure.

$$P_{+,0}=+hd+b_1^2+b_2^2, \tag{32}$$

$$P_{+,1}=-hd+b_1^2-b_2^2+b_2, \tag{33}$$

$$P_{+,2}=-hd-b_1^2+b_1+b_2^2, \tag{34}$$

$$P_{+,3}=+hd-b_1^2+b_1-b_2^2+b_2, \tag{35}$$

$$P_{-,0}=-hd-b_1^2+b_1-b_2^2+b_2, \tag{36}$$

$$P_{-,1}=+hd-b_1^2+b_1+b_2^2, \tag{37}$$

$$P_{-,2}=+hd+b_1^2-b_2^2+b_2, \tag{38}$$

$$P_{-,3}=-hd+b_1^2+b_2^2. \tag{39}$$

As special cases, the result for two square layers (2□) is obtained by requiring equality of both lateral lattice constants, $b_1=b_2$. For one triangular layer (1△), the vertical layer spacing is set to zero ($d=0$), and the ratio of the lateral lattice constants is that of an equilateral triangle, hence $b_1=b_2\sqrt{3}/2$.

A modification is done for the description of the 1△ phase [72], where we inserted a different effective diameter $\sigma_{1\triangle}^*=\sigma\sqrt{1-h^2/6}$ into the expression for the 1△ free volume in order to enlarge the free volume for two touching spheres with different z coordinates. This is further justified at the end of Sec. V B. For the rhombic and 2△ phases, we rely on a numerical strategy, details of which are given in Ref. [70].

Both the analytical and numerical solutions for the free energy still depend on a set of free parameters. The buckling structure depends on the ratio of lattice constants a_1/a_2 and on the layer spacing d. The rhombic structure depends also on d and on the angle of the rhombus. To optimize the upper bound on the free energy, we numerically maximize the free volume v_f with respect to the free lattice parameters. An interesting point concerns the stability of the linear buckling with respect to the zigzag buckling phase. Remember that the former is built up from rectangles, while the latter is composed of kites. A kite contains one additional degree of freedom, namely, the position of the center on the symmetry axis. It turns out that the maximal free volume for the kite is attained if it equals the free volume of the rectangle. Thus within the cell model both phases are equally stable, even away from close packing.

B. Effective-diameter liquid theory

We now focus on the fluid state. For large plate separations a theory was established using the Percus shielding approximation [82], which can be solved analytically

[83,84]. Here we present a theory that predicts the equation of state and the density profile of the confined hard sphere fluid in the complementary regime of small plate separations.

The idea is to map the confined system onto well-known strictly two-dimensional hard disks with an effective particle diameter σ^*. To determine the effective diameter, our starting point is the Born-Green-Yvon (BGY) hierarchy [85], applied to an inhomogeneous situation with nonvanishing external potential [86]. In order to close the BGY hierarchy, we approximate the inhomogeneous pair correlation function at contact by a constant, which is taken self-consistently from the 2D hard disk equation of state, given within scaled-particle theory [87,88]. We present an analytical solution for $H<2\sigma$ as well as explicit expressions for the density profile and the equation of state.

In a liquid exposed to a nonvanishing external potential $V_{\rm ext}(\mathbf{r})$, the BGY hierarchy relates the single-particle density $\rho(\mathbf{r})$ to the pair distribution function $g(\mathbf{r},\mathbf{r}')$ as follows [86]:

$$-k_BT\nabla\ \ln\rho(\mathbf{r})=\nabla V_{\rm ext}(\mathbf{r})+\int d\mathbf{r}'\rho(\mathbf{r}')g(\mathbf{r},\mathbf{r}')\nabla V(\mathbf{r},\mathbf{r}'). \tag{40}$$

Here $V(\mathbf{r},\mathbf{r}')$ is the pair interaction potential and $\nabla\equiv\partial/\partial\mathbf{r}$. In the case of hard spheres confined in a hard external potential (which only takes on the values zero or infinity), Eq. (40) can be written as

$$\nabla\ln\rho(\mathbf{r})=\sigma^{-1}\int d\mathbf{r}'\rho(\mathbf{r}')g(\mathbf{r},\mathbf{r}') \times\delta(|\mathbf{r}-\mathbf{r}'|-\sigma)(\mathbf{r}-\mathbf{r}') \quad \text{if}\ \ V_{\rm ext}(\mathbf{r})=0, \tag{41}$$

$$\rho(\mathbf{r})=0 \quad \text{if}\ \ V_{\rm ext}(\mathbf{r})=\infty. \tag{42}$$

A simplification arises from the presence of the δ function on the right-hand side of Eq. (41), so that only the pair correlations $g(\mathbf{r},\mathbf{r}')$ *at contact*, i.e., $|\mathbf{r}-\mathbf{r}'|=\sigma$ enter in the determination of the one-particle density distribution.

In the case of parallel planar walls, due to symmetry, the fluid density profile depends only on the coordinate z perpendicular to the walls, $\rho(\mathbf{r})=\rho(z)$ while the pair distribution depends on both z coordinates and on the magnitude $r=|\mathbf{r}-\mathbf{r}'|$, hence $g(\mathbf{r},\mathbf{r}')=g(z,z',r)$. In order to reduce the notational effort, we define $h'=h\sigma,\rho_0=N/(Ah')=h/(h+1)\rho_H\sigma^{-3}$, and pressures $\Pi_{\rm lat}=-(h')^{-1}\partial F/\partial A$, and $\Pi_{\rm trans}=-A^{-1}\partial F/\partial h'$.

Transforming Eq. (41) to cylindrical coordinates, we obtain the following exact nonlinear integrodifferential equation for the density profile:

$$\frac{d}{dz}\ln\rho(z)=2\pi\int_{z-\sigma}^{z+\sigma}dz'\ \rho(z')g(z,z',\sigma)(z-z'). \tag{43}$$

Alternatively, Eq. (43) can be written in pure integral form,

$$\rho(z)=\rho_{\rm W}-2\pi\int_{z-\sigma}^{z}dz_1\ \ \rho(z_1) \times\int_{z}^{z_1+\sigma}dz_2\ \ \rho(z_2)(z_2-z_1)g(z_1,z_2,\sigma), \tag{44}$$

where the wall contact density is defined as

$$\rho_{\rm W}:=\rho(+h'/2)=\rho(-h'/2). \tag{45}$$

Once the density profile is known, the lateral and transversal pressures can be computed (see Appendix A) via

$$\beta\Pi_{\rm lat}=\rho_0+\frac{\pi}{2h'}\int_{-h'/2}^{+h'/2}dz_1\ \ \rho(z_1)\int_{z_1-\sigma}^{z_1+\sigma}dz_2\ \ \rho(z_2) \times[\sigma^2-(z_2-z_1)^2]g(z_1,z_2,\sigma), \tag{46}$$

$$\beta\Pi_{\rm trans}=\rho_0+\frac{\pi}{h'}\int_{-h'/2}^{+h'/2}dz_1\ \ \rho(z_1) \times\int_{z_1-\sigma}^{z_1+\sigma}dz_2\ \ \rho(z_2)(z_2-z_1)^2g(z_1,z_2,\sigma). \tag{47}$$

The ideal-gas contribution is

$$\rho_0:=\frac{1}{h'}\int_{-h'/2}^{+h'/2}dz\ \ \rho(z), \tag{48}$$

Of course, the set of equations (43), (46), and (47) is not a closed one, as the inhomogeneous contact pair distribution $g(z,z',\sigma)$ is in general unknown. A closure approximation is estabished by an *effective-diameter approximation*. First, we neglect the spatial dependence of the pair distribution function

$$g(\rho_0;z_1,z_2,\sigma)\approx g^*(\rho_0), \tag{49}$$

and second, we propose a self-consistent scheme for the determination of g^* as a function of the thermodynamic variable ρ_0 as follows:

We restrict ourselves to a narrow gap with $h'<\sigma$. In this regime, due to the vanishing density outside the gap [Eq. (42)] the integration limits in the z' integral in Eq. (43) and in the z_2 integrals in Eqs. (46) and (47) are significantly simplified to $[-h'/2,h'/2]$.

The density profile can be calculated analytically via Eq. (43), which reads under the approximation (49)

$$\frac{d}{dz}\ln\rho(z)=2\pi\int_{-h'/2}^{+h'/2}dz'\ \rho(z')g(z,z',\sigma)(z-z') \tag{50}$$

$$\approx 2\pi g^*(\rho_0)\int_{-h'/2}^{+h'/2}dz'\ \rho(z')(z-z') \tag{51}$$

$$=2\pi g^*(\rho_0)\rho_0h'z. \tag{52}$$

The solution is

$$\rho(z)=\frac{\rho_0h'}{\mathcal{N}}\exp[\alpha(\rho_0)z^2], \tag{53}$$

$$\mathcal{N}=\sqrt{\pi/\alpha(\rho_0)}\ \ \mathrm{erfi}\left(\frac{\sqrt{\alpha(\rho_0)}h'}{2}\right), \tag{54}$$

$$\alpha(\rho_0)=\pi\rho_0h'g^*(\rho_0), \tag{55}$$

the imaginary error function is given by $\mathrm{erfi}(z)=\pi^{-1/2}\int_{-z}^{z}dz'\ \exp z'^2$. The lateral compressibility is obtained through Eq. (46),

$$\frac{\beta\Pi_{\mathrm{lat}}}{\rho_0}=1+\frac{\pi}{2}\rho_0 h' g^*(\rho_0)[\sigma^*(\rho_0)]^2, \tag{56}$$

$$[\sigma^*(\rho_0)]^2\equiv\sigma^2-\int_{-h'/2}^{h'/2}dz_1\frac{\rho(z_1)}{\rho_0 h'}\times\int_{-h'/2}^{h'/2}dz_2\frac{\rho(z_2)}{\rho_0 h'}(z_1-z_2)^2, \tag{57}$$

where we have defined an effective diameter σ^*. It can be calculated explicitly by inserting the density profile given by Eqs. (53)–(55) into Eq. (57). The result is

$$[\sigma^*(\rho_0)]^2=\sigma^2+\frac{1}{\alpha(\rho_0)}-\frac{h'\ \exp[\alpha(\rho_0)\ h'^2/4]}{\sqrt{\pi\ \alpha(\rho_0)}\ \mathrm{erfi}[\sqrt{\alpha(\rho_0)}\ h'/2]}. \tag{58}$$

Having solved for the density profile, we are left with the problem of approximate determination of the function $g^*(\rho_0)$. As a functional form for g^* we use the expression from 2D scaled-particle theory [87], which is in sufficiently reasonable agreement with Monte Carlo data [89]

$$g^*(\rho_0)=\frac{1-\frac{1}{2}\eta^*(\rho_0)}{[1-\eta^*(\rho_0)]^2}. \tag{59}$$

The problem is thereby carried over to the determination of an effective 2D packing fraction η^* of the slab system dependent on the average density ρ_0. Comparing the lateral compressibility, Eq. (56), with the 2D virial theorem, we make the plausible assumption to build up a 2D packing fraction with the effective diameter σ^*,

$$\eta^*(\rho_0)=\frac{\pi}{4}\rho_0 h'[\sigma^*(\rho_0)]^2. \tag{60}$$

Inserting Eq. (60) into Eq. (59) yields, together with Eqs. (55) and (58), the desired relation between g^* and ρ_0; it is an implicit equation for the determination of the function $g^*(\rho_0)$. The solution can be used to compute the excess free energy via integration of the scaled-particle 2D compressibility

$$\beta f_{\mathrm{ex}}(\rho_0)=\int_0^{\rho_0}\frac{d\rho_0'}{\rho_0'}[Z_{\mathrm{SPT}}(\rho_0')-1], \tag{61}$$

$$Z_{\mathrm{SPT}}(\rho_0)=\frac{1}{[1-\eta^*(\rho_0)]^2}. \tag{62}$$

Let us finally justify the insertion of an effective diameter into the expression for the cell model result for the $1\triangle$ phase. An effective 2D disk diameter is obtained through Eq. (57) once the density profile is known. As the $1\triangle$ free-volume cell is a hexagonal prism the density profile is constant with respect to the transverse z coordinate. Hence Eq. (57) becomes

$$[\sigma^*(\rho_0)]^2=\sigma^2-\int_{-h\sigma/2}^{h\sigma/2}dz_1\int_{-h\sigma/2}^{h\sigma/2}dz_2(z_1-z_2)^2 \tag{63}$$

$$=\sigma^2-\frac{\sigma^2h^2}{6}. \tag{64}$$

Via this modification, the effect that two spheres with different z coordinates can come laterally closer than their hard sphere diameter is taken into account.

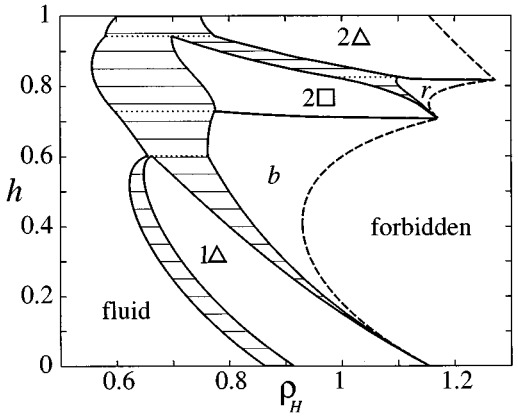

FIG. 16. Cell theory result for the phase diagram of hard spheres of density ρ_H confined between parallel plates with separation distance h. Six phases occur (fluid, $1\triangle$, b, $2\square$, r, and $2\triangle$.) The closed-packed density is marked by a dashed line. Thin horizontal lines represent two-phase coexistence, and dotted lines represent situations with three coexisting phases. To be compared with the MC simulation result shown in Fig. 4.

C. Phase diagram and discussion

In Fig. 16 the theoretical phase diagram of confined hard spheres is presented. It is calculated using the cell model description of the solid phases and the effective-diameter approximation for the liquid phase. The theoretical predictions are to be compared with the simulated phase diagram shown in Fig. 4.

The agreement for $h=0$ (hard disks) is enforced by adding the suitably chosen constant $C=1.8$ to all solid entropies. As all solid free energies are shifted by the same amount, solid-solid coexistence is unaffected by the introduction of the fitting constant C.

The shapes and the positions of the f-$1\triangle$ and $1\triangle$-b coexistence regions are in pretty good agreement with the simulations. Also the disappearance of the $1\triangle$-b region toward the high-density limit as $h\to 0$ is captured correctly. However, for values $0.6<h<0.72$, a strongly first-order fluid-buckling freezing transition appears, which does not match the simulation. Also, the slope of the b-$2\square$ coexistence line is negative in cell theory, but is positive in simulation. (This implies a *high-density* buckling phase in coexistence with a *low-density* square phase in reality.) The

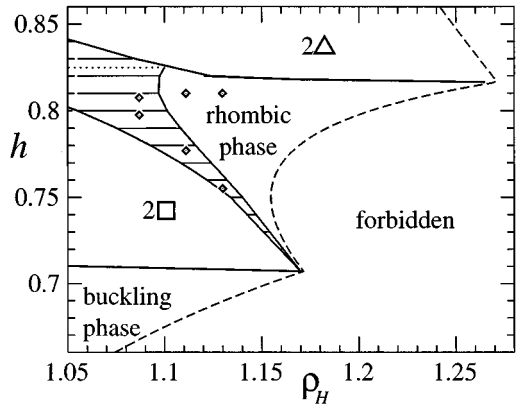

FIG. 17. Enlargement of Fig. 16. The MC data are shown as points.

density gap between the $2\square$ and the buckling phase is miniscule, e.g., $\Delta\rho_H = 0.000\ 47$ at $h = 0.72$, compatible with the simulation. The agreement of the fluid-solid coexistence grows worse as h increases further up to unity, as we map a multilayer fluid onto a single-layer fluid. The $2\square$-r density jump is overestimated, but the weakness of the $2\triangle$-r transition is predicted correctly. As in the case of the b-$2\square$ transition the slopes of the $2\triangle$-r lines have the wrong sign (see also the detailed plot in Fig. 17). The relative extent of stability of both close-packed phases, b and r, is in agreement with MC data. In conclusion, while the topology of the phase diagram is reproduced correctly, the overall agreement is only semiquantitative, since some details are not predicted correctly.

A final remark concerns three-phase coexistence: In the 2D and 3D bulk limits, the Gibbs phase rule permits two coexisting phases, as there is only one free thermodynamic variable, namely, the density. The existence of surfaces changes this result, due to the additional freedom introduced by the transversal pressure. In the ensemble of prescribed wall separation distance the pure phases will in general exert different pressures on the plates. Hence a state with three coexisting phases can be uniquely decomposed into the pure phases if the average density and and transversal pressure are known.

VI. CONCLUSION

In conclusion, we investigated the freezing transition in confining geometry focusing on the hard sphere model confined between parallel plates. We demonstrated that freezing is drastically affected by confinement. Because of the inhomogeneity, the uniqueness of the (close-packed) crystalline state is lost and a cascade of different solids compete for the thermodynamically stable state. The close-packed configurations are also thermodynamically stable at lower densities away from close packing, and nontrivial phase transformations are encountered between phases where the particles can be very efficiently packed in space, and phases that exhibit less efficient packing, but possess higher symmetries.

With Monte Carlo computer simulation we have shown that, besides the strongly discontinuous freezing transition of the confined fluid, there occur both very weak and strong first-order phase transitions between different crystalline structures. In particular, the transition from two square crystalline layers to the buckling structure was investigated in detail. Symmetry considerations cannot rule out a continuous transition, and no van der Waals loop could be resolved from the equation of state. However, the order parameter fluctuations measured by means of a susceptibility remain finite as the phase transition is approached. This observation is consistent with a first-order transition.

The data from computer simulations were compared with free-volume theory, consisting of a cell model for the crystalline states and a mapping based on the BGY hierarchy of the fluid phase in slab geometry on an effective 2D hard disk system. This approach is able to achieve striking similarities for the topology of the confined hard sphere phase diagram. Even a partial quantitative agreement was found. The density jumps are generally overestimated, but are of the correct order. The prediction for the freezing transition grows worse with increasing plate separation distance and the slopes of some solid-to-solid coexistence lines have the wrong sign. In these cases correlation effects must be considered in a more sophisticated way. The model can be generalized in different directions, a detailed discussion is given in Ref. [65].

As an outlook, it would be highly desirable to verify our theoretical predictions experimentally in samples of sterically stabilized or highly salted colloidal suspensions. Work along this line is in progress [20].

Furthermore, it would be interesting to apply density-functional theory of freezing to the confined hard sphere system. In particular, Rosenfeld's hard sphere functional [90] should give relieable data in a situation between three and two spatial dimensions [91,92].

ACKNOWLEDGMENTS

We thank H. Wagner, Y. Rosenfeld, A. Hüller, M. Promberger, P. Leiderer, T. Palberg, S. Neser, A. Denton, and R. Bausch for helpful discussions. This work was supported by the Deutsche Forschungsgemeinschaft within the Gerhard-Hess Programm.

APPENDIX A: PRESSURES

In the following an efficient means of calculating the lateral and transversal pressures by computer simulation is presented. It is based on the relation of the pressure for hard particles to the probability density of a successful infinitesimal volume contraction of the whole system. We introduce the concept of a system volume being scaled in d directions by a factor ξ. Two different scalings of the system are considered: (i) scaling of the $d=2$ lateral directions, $(\xi L_x, \xi L_y, h\sigma)$; and (ii) scaling of the $d=1$ transversal box height, $(L_x, L_y, \xi h\sigma)$. The system volume is $V(\xi) = \xi^d L_x L_y h\sigma$, where $d=1$ and 2. We define a ξ-dependent configurational integral for hard spheres as

$$Q(\xi) = \frac{1}{N!}\int_{V(\xi)} d\mathbf{r}_1 \cdots \int_{V(\xi)} d\mathbf{r}_N \prod_{i<j} \Theta(|\mathbf{r}_i - \mathbf{r}_j| - \sigma). \tag{A1}$$

Note that the Boltzmann factor for hard spheres can be written as a product of Heaviside functions Θ. For $\xi=1$ we recover the usual configurational integral.

Now the pressure can be expressed as a derivative with respect to ξ, namely,

$$\beta P \equiv \frac{\partial \ln Q}{\partial V} \tag{A2}$$

$$= \left[\frac{1}{Q} \frac{\partial Q(\xi)}{\partial \xi} \left(\frac{\partial V(\xi)}{\partial \xi} \right)^{-1} \right]_{\xi=1}. \tag{A3}$$

To calculate $\partial Q/\partial \xi$ we rewrite Eq. (A1),

$$Q(\xi) = \frac{1}{N!} \xi^{Nd} \int_{V(1)} d\mathbf{r}_1 \cdots \int_{V(1)} d\mathbf{r}_N \prod_{i<j}{}' \ \Theta(|\mathbf{r}_{ij}(\xi)| - \sigma), \tag{A4}$$

where $\mathbf{r}_{ij}(\xi) \equiv \mathbf{r}_i(\xi) - \mathbf{r}_j(\xi)$, and scaled coordinates are used: (i) $\mathbf{r}_i(\xi) = (\xi x_i, \xi y_i, z_i)$, and (ii) $\mathbf{r}_i(\xi) = (x_i, y_i, \xi z_i)$.

Then the derivative is

$$\frac{\partial Q}{\partial \xi} = Nd\xi^{Nd-1} Q + \frac{1}{N!} \int_{V(1)} d\mathbf{r}_1 \cdots \int_{V(1)} d\mathbf{r}_N \times \sum_{k<l} \delta[|\mathbf{r}_{kl}(\xi)| - \sigma] \frac{\partial |\mathbf{r}_{kl}(\xi)|}{\partial \xi} \prod_{i<j}{}' \ \Theta(|\mathbf{r}_{ij}(\xi)| - \sigma), \tag{A5}$$

the prime at the product symbol denotes omission of the pair (k,l). We further calculate

$$\left[\frac{1}{Q} \frac{\partial Q}{\partial \xi} \right]_{\xi=1} = Nd + \left\langle \sum_{k<l} \delta[|\mathbf{r}_{kl}(\xi)| - \sigma] \frac{\partial |\mathbf{r}_{kl}(\xi)|}{\partial \xi} \right\rangle_{\xi=1} \tag{A6}$$

$$= Nd + \left\langle \sum_{k<l} \delta(\xi_{kl} - \xi) \right\rangle_{\xi=1}, \tag{A7}$$

where ξ_{kl} is defined through $\mathbf{r}_{kl}(\xi_{kl}) = \sigma$. Distinguishing between the lateral ($d=2$), and the transversal case ($d=1$) we obtain the rescaling factors that bring the particles in contact with each other,

$$\xi_{\mathrm{lat},kl} = \left(\frac{\sigma^2 - z_{kl}^2}{x_{kl}^2 + y_{kl}^2} \right)^{1/2}, \tag{A8}$$

$$\xi_{\mathrm{trans},kl} = \left(\frac{\sigma^2 - (x_{kl}^2 + y_{kl}^2)}{z_{kl}^2} \right)^{1/2}, \tag{A9}$$

and, using Eqs. (A7) and (A3), we obtain

$$\frac{\beta p_{\mathrm{lat}}}{\rho_H} = 1 + \frac{1}{2} \left\langle \frac{1}{N} \sum_{k<l} \delta(\xi - \xi_{\mathrm{lat},kl}) \right\rangle_{\xi=1}, \tag{A10}$$

$$\frac{h}{h+1} \frac{\beta p_{\mathrm{trans}}}{\rho_H} = 1 + \left\langle \frac{1}{N} \sum_{k<l} \delta(\xi - \xi_{\mathrm{trans},kl}) \right\rangle_{\xi=1}. \tag{A11}$$

The ideal gas contribution to the total pressure is given by the summand 1 after the equality signs. During the Monte Carlo simulation the canonical averages are calculated for $\xi<1$ and then extrapolated, $\xi \to 1$. It should be noted that the procedure is mainly important for the lateral case, as the transversal pressure can readily be calculated via the wall theorem [38].

Concerning the fluid free-volume theory, Eqs. (46) and (47) are derived from Eq. (A5) by noting that, at contact, $|\mathbf{r}_{12}| = \sigma$, for the lateral case

$$\left. \frac{\partial}{\partial \xi} |\mathbf{r}_{12}(\xi)| \right|_{\xi=1} = \frac{\sigma^2 - (z_1 - z_2)^2}{\sigma} \tag{A12}$$

and for transversal cases

$$\left. \frac{\partial}{\partial \xi} |\mathbf{r}_{12}(\xi)| \right|_{\xi=1} = \frac{(z_1 - z_2)^2}{\sigma}, \tag{A13}$$

is obeyed.

APPENDIX B: PRESSURE ENSEMBLE

The discussion in Sec. IV B makes use of the canonical ensemble (NVT). One encounters different behavior of the susceptibility for discontinuous and continuous phase transitions in the pressure ensemble ($Np_{\mathrm{lat}}T$) and in the grand canonical ensemble (μVT). Moreover, in each of the ensembles apart from the natural variables, the susceptibility can be regarded as a function of the conjugated variable, e.g., in (NVT) as a function of the pressure p_{lat}. We focus on the ($Np_{\mathrm{lat}}T$) case, the grand canonical case being similar.

The pressure ensemble is related to the constant volume ensemble via the Laplace transform

$$\chi_{mn}^{(p_{\mathrm{lat}})}(p_{\mathrm{lat}}) = \int dV \chi_{mn}^{(V)}(V) e^{-\beta[p_{\mathrm{lat}} V - F(V)]}. \tag{B1}$$

For a continuous phase transition, the common case is a power-law divergence of both susceptibilities:

$$\chi_{mn}^{(p_{\mathrm{lat}})}(p_{\mathrm{lat}}) \propto |p_{\mathrm{lat}} - p_{\mathrm{crit}}|^{-\alpha}, \tag{B2}$$

$$\chi_{mn}^{(V)}(\rho_H) \propto |\rho_H - \rho_{\mathrm{crit}}|^{-\alpha'}, \tag{B3}$$

with positive critical exponents α and α'. For the discontinuous case, the behavior of both quantities differs markedly

$$\chi_{mn}^{(p_{\mathrm{lat}})}(P_{\mathrm{lat}}) \propto (\rho_H^{(2)} - \rho_H^{(1)}) \delta(P_{\mathrm{lat}} - p_{\mathrm{crit}}), \tag{B4}$$

$$\chi_{mn}^{(V)}(\rho_H) = \lambda \chi_{mn}^{(V)}(\rho_H^{(1)}) + (1-\lambda) \chi_{mn}^{(V)}(\rho_H^{(2)}). \tag{B5}$$

[1] J. Perrin, Ann. Chim. Phys. **18**, 1 (1909); see also [23].
[2] J. S. Rowlinson and B. Widom, *Molecular Theory of Capillarity* (Clarendon, Oxford, 1982).
[3] M. Schoen, D. J. Diestler, and J. H. Cushman, J. Chem. Phys. **101**, 6865 (1994).
[4] M. Krech, *The Casimir Effect in Critical Systems* (World Scientific, Singapore, 1995).
[5] P. A. Thompson, G. S. Grest, and M. O. Robbins, Phys. Rev. Lett. **68**, 3448 (1992).
[6] H. K. Christenson, Phys. Rev. Lett. **74**, 4675 (1995).
[7] H. M. Fretwell, J. A. Duffy, A. P. Clarke, M. A. Alam, and R. Evans, J. Phys. Condens. Matter **8**, 9613 (1996).
[8] See, e.g., A. Demirel and S. Granick, Phys. Rev. Lett. **77**, 2261 (1996).
[9] T. Fehr and H. Löwen, Phys. Rev. E **52**, 4016 (1995).
[10] J. Baschnagel and K. Binder, J. Phys. (France) I **6**, 1271 (1996).
[11] L. Bocquet and J. L. Barrat, J. Phys. Condens. Matter **8**, 9297 (1996).
[12] M. Schoen and M. Thommes, Phys. Rev. E **52**, 6375 (1995).
[13] T. Chou and D. R. Nelson, Phys. Rev. E **48**, 4611 (1993).
[14] T. Chou and D. R. Nelson, Phys. Rev. E **53**, 2560 (1996).
[15] P. Pieranski and L. Strzelecki, Phys. Rev. Lett. **50**, 331 (1983).
[16] D. H. Van Winkle and C. A. Murray, Phys. Rev. A **34**, 562 (1986).
[17] C. A. Murray, W. O. Sprenger, and R. A. Wenk, Phys. Rev. B **42**, 688 (1990).
[18] C. A. Murray, in *Bond-Orientational Order in Condensed Matter Systems*, edited by K. J. Strandburg (Springer, New York, 1992).
[19] J. Weiss, D. W. Oxtoby, D. G. Grier, and C. A. Murray, J. Chem. Phys. **103**, 1180 (1995).
[20] S. Neser, T. Palberg, and P. Leiderer, Prog. Col. Polym. Sci. (to be published).
[21] T. Ogawa, J. Phys. Soc. Jpn. Suppl. **52**, 167 (1983).
[22] M. Giersig and P. Mulvaney, Langmuir **9**, 3408 (1993).
[23] N. D. Denkov, O. D. Velev, P. A. Kralchevsky, I. B. Ivanov, H. Yoshimura, and K. Nagayama, Langmuir **8**, 3183 (1992).
[24] C. D. Dushkin, K. Nagayama, T. Miwa, and P. A. Kralchevsky, Langmuir **9**, 3695 (1993).
[25] P. Pieranski, Phys. Rev. Lett. **45**, 569 (1980).
[26] K. Zahn, R. Lenke, and G. Maret (unpublished).
[27] J. Mendez-Alcaraz, K. Zahn, and G. Maret (unpublished).
[28] H. Thomas, G. E. Morfill, V. Demmel, J. Goree, B. Feuerbacher, and D. Möhlmann, Phys. Rev. Lett. **73**, 652 (1994).
[29] G. E. Morfill and H. Thomas, J. Vac. Sci. Technol. A **14**, 490 (1995).
[30] H. Thomas and G. E. Morfill, J. Vac. Sci. Technol. A **14**, 501 (1995).
[31] F. M. Peeters, V. A. Schweigert, and V. M. Bedanov, Physica A **212**, 237 (1995).
[32] G. Goldoni and F. M. Peeters, Phys. Rev. B **53**, 4591 (1996).
[33] G. Goldoni and F. M. Peeters (unpublished).
[34] F. M. Peeters and X. Wu, Phys. Rev. A **35**, 3109 (1987).
[35] S. Narasimhan and T.-H. Ho, Phys. Rev. B **52**, 12 291 (1995).
[36] L. Zheng and H. A. Fertig, Phys. Rev. B **52**, 12 282 (1995).
[37] M. Schmidt and H. Löwen, Phys. Rev. Lett. **76**, 4552 (1996).
[38] I. Z. Fisher, *Statistical Theory of Liquids* (University of Chicago Press, Chicago, 1964).
[39] B. C. Freasier, C. E. Woodward, and S. Nordholm, J. Chem. Phys. **90**, 5657 (1989).
[40] R. Leidl and H. Wagner, J. Chem. Phys. **98**, 4142 (1993).
[41] B. Götzelmann, A. Haase, and S. Dietrich, Phys. Rev. E **53**, 3456 (1996).
[42] D. Henderson, F. F. Abraham, and J. A. Barker, Mol. Phys. **31**, 1291 (1976).
[43] D. Henderson, in *Fundamentals of Inhomogeneous Fluids*, edited by D. Henderson (Marcel Dekker, New York, 1992).
[44] R. Ohnesorge, H. Löwen, and H. Wagner, Phys. Rev. E **50**, 4801 (1994).
[45] D. J. Courtemanche and F. van Swol, Phys. Rev. Lett. **69**, 2078 (1992).
[46] D. J. Courtemanche, T. A. Pasmore, and F. van Swol, Mol. Phys. **80**, 861 (1993).
[47] D. J. Diestler, M. Schoen, and J. H. Cushman, Science **262**, 545 (1993).
[48] B. Götzelmann and S. Dietrich, Phys. Rev. E **55**, 2993 (1997).
[49] J. E. Hug, F. van Swol, and C. F. Zukoski, Langmuir **11**, 111 (1995).
[50] *Molecular Dynamics in Restricted Geometries*, edited by J. Klafter and J. M. Drake (Wiley, New York, 1989).
[51] W. Schaertl and H. Sillescu, J. Stat. Phys. **77**, 1007 (1994).
[52] K. J. Strandburg, Rev. Mod. Phys. **60**, 161 (1988).
[53] J. Lee and K. J. Strandburg, Phys. Rev. B **46**, 11 190 (1992).
[54] J. A. Zollweg, G. V. Chester, and P. W. Leung, Phys. Rev. B **46**, 11 186 (1992).
[55] J. F. Fernández, J. J. Alonso, and J. Stankiewicz, Phys. Rev. Lett. **75**, 3477 (1995).
[56] H. Weber and D. Marx, Europhys. Lett. **27**, 593 (1994).
[57] H. Weber, D. Marx, and K. Binder, Phys. Rev. B **51**, 14 636 (1995).
[58] J. J. Erpenbeck and W. W. Wood, J. Stat. Phys **35**, 321 (1984).
[59] J. J. Erpenbeck and M. Luban, Phys. Rev. A **32**, 2920 (1985).
[60] B. Pansu, P. Pieranski, and P. Pieranski, J. Phys. (Paris) **45**, 331 (1984).
[61] R. R. Netz, in *The Structure and Conformation of Amphiphilic Membranes*, edited by R. Lipowsky, D. Richter, and K. Kremer, Springer Proceedings in Physics Vol. 66 (Springer-Verlag, Berlin, 1992), p. 61.
[62] C. Cametti, F. D. Luca, A. D'Illario, G. Briganti, and M. A. Macri, in *The Structure and Conformation of Amphiphilic Membranes*, edited by R. Lipowsky, D. Richter, and K. Kremer, Springer Proceedings in Physics Vol. 66 (Springer-Verlag, Berlin, 1992), p. 66.
[63] D. Rüppel and E. Sackmann, J. Phys. (Paris) **44**, 1025 (1983).
[64] A. Saint-Jalmes, F. Graner, and F. Gallet, Europhys. Lett. **28**, 565 (1994).
[65] H. Löwen and M. Schmidt, Prog. Colloid Polym. Sci. (to be published).
[66] M. P. Allen and D. J. Tildesley, *Computer Simulation of Liquids* (Oxford University Press, Oxford, 1987).
[67] W. G. Hoover and F. H. Ree, J. Chem. Phys. **49**, 3609 (1968).
[68] W. G. Hoover and F. H. Ree, J. Chem. Phys. **47**, 4837 (1967).
[69] D. Frenkel and A. J. C. Ladd, J. Chem. Phys. **81**, 3188 (1984).
[70] M. Schmidt, Ph.D. thesis, Heinrich-Heine Universität Düsseldorf, 1997.
[71] N. B. Wilding and K. Binder, Physica A **231**, 439 (1996).
[72] A. Bonissent, P. Pieranski, and P. Pieranski, Philos. Mag. A **50**, 57 (1984).
[73] W. W. Wood, J. Chem. Phys. **20**, 1334 (1952).
[74] J. G. Kirkwood, J. Chem. Phys. **18**, 380 (1950).
[75] K. W. Wojciechowski, Phys. Lett. A **122**, 377 (1987).
[76] F. L. Somer and J. Kovac, J. Chem. Phys. **102**, 8995 (1995).

[77] M. P. Taylor, R. Hentschke, and J. Herzfeld, Phys. Rev. Lett. **62**, 800 (1989).
[78] H. Graf, H. Löwen, and M. Schmidt, Prog. Colloid Polym. Sci. (to be published).
[79] A. R. Denton, N. W. Ashcroft, and W. A. Curtin, Phys. Rev. E **51**, 65 (1995).
[80] F. H. Stillinger, Jr. and Z. W. Salsburg, J. Stat. Phys. **1**, 179 (1969).
[81] J. A. Barker, J. Chem. Phys. **63**, 632 (1975).
[82] J. K. Percus, J. Stat. Phys. **23**, 657 (1980).
[83] M. S. Wertheim, J. Chem. Phys. **84**, 2808 (1986).
[84] M. S. Wertheim, L. Blum, and D. Bratko, in *Micellar Solutions and Microemulsions: Structure, Dynamics and Statistical Thermodynamics*, edited by S.-H. Chen and R. Rajagopalan (Springer-Verlag, New York, 1990).
[85] M. Born and M. S. Green, *A General Kinetic Theory of Liquids* (Cambridge University Press, Cambridge, 1949).
[86] J. P. Hansen and I. R. McDonald, *Theory of Simple Liquids*, 2nd ed. (Academic, London, 1986).
[87] E. Helfand, H. L. Frisch, and J. L. Lebowitz, J. Chem. Phys. **34**, 1037 (1961).
[88] H. Reiss, H. L. Frisch, and J. L. Lebowitz, J. Chem. Phys. **31**, 369 (1959).
[89] A. Santos, M. L. de Haro, and S. B. Yuste, J. Chem. Phys. **103**, 4622 (1995).
[90] Y. Rosenfeld, Phys. Rev. A **42**, 5978 (1990).
[91] Y. Rosenfeld, M. Schmidt, H. Löwen, and P. Tarazona, J. Phys. Condens. Matter **8**, L577 (1996).
[92] Y. Rosenfeld, J. Phys. Condens. Matter **8**, L795 (1996).